Machine Learning Prediction of the Experimental Transition Temperature of Fe(II) Spin-Crossover Complexes

Vyshnavi Vennelakanti[1,2], Irem B. Kilic[1], Gianmarco G. Terrones[1,2], Chenru Duan[1,2], and Heather J. Kulik[1,2],*

[1]*Department of Chemical Engineering, Massachusetts Institute of Technology, Cambridge, MA 02139, USA*
[2]*Department of Chemistry, Massachusetts Institute of Technology, Cambridge, MA 02139, USA*

*Corresponding author email: hjkulik@mit.edu phone: 617-253-4584

ABSTRACT: Spin crossover (SCO) complexes are materials that exhibit changes in spin state in response to external stimuli with potential applications in molecular electronics. It is challenging to know a priori how to design ligands to achieve the delicate balance of entropic and enthalpic contributions needed to tailor a transition temperature close to room temperature. We leverage the SCO complexes from the previously curated SCO-95 data set [Vennelakanti et al. *J. Chem. Phys.* **159**, 024120 (2023)] to train three ML models for transition temperature ($T_{1/2}$) prediction, using graph-based revised autocorrelations as features. We perform feature selection using random forest-ranked recursive feature addition (RF-RFA) to identify the features essential to model transferability. Of the ML models considered, the full feature set random forest (RF) and recursive feature addition RF models perform best, achieving moderate correlation to experimental $T_{1/2}$ values. We then compare ML $T_{1/2}$ predictions to those from three previously identified best-performing density functional approximations (DFAs) which accurately predict SCO behavior across SCO-95, finding that the ML models predict $T_{1/2}$ more accurately than the best-performing DFAs. In addition, we study ML model predictions on the set of 18 SCO complexes for which only estimated $T_{1/2}$ values are available. Upon excluding outliers from this set, the RF-RFA RF model shows strong correlation to estimated $T_{1/2}$ values with a Pearson's r of 0.82. In contrast, DFA-predicted $T_{1/2}$ values have large errors and show no correlation to estimated $T_{1/2}$ values over the same set of complexes. Overall, our study demonstrates reasonable performance of ML models in comparison to some of the best-performing DFAs, and we expect ML models to improve further as larger data sets of SCO complexes are curated and become available for model training.

1. Introduction.

Spin crossover (SCO) complexes[1-3] exhibit a change in spin state from low-spin (LS) to high-spin (HS) or vice versa, as a function of external stimuli[4] like temperature[5,6], pressure[1,5-8], or light[7,9-12]. These complexes find a variety of applications[13] in molecular spintronics[14], memory devices[15], sensors[16], optical devices[17], and displays[18]. Fe(II) SCO complexes with nitrogen-coordinating ligands are studied extensively[19] since they exhibit greatest structural differences between HS and LS states,[20-25] allowing for clear distinction between the two spin states and leading to better switching properties in molecular memory devices. A multitude of experimental techniques such as magnetic susceptibility measurements,[26-28] Mössbauer spectroscopy,[26-28] variable-temperature IR[29-31] and NMR,[31-33] UV/Vis,[32-34] Raman,[30,31,35] and X-ray crystallography,[26-28] are employed to characterize SCO behavior. While experimental techniques characterize SCO behavior through structural changes and measurement of transition temperature ($T_{1/2}$), it remains challenging[3,36,37] to tailor SCO $T_{1/2}$ for use in molecular devices[25]. Computational investigations[12,37-42] of SCO behavior aim to bridge the gaps in experimental studies of SCO complexes.

Computational predictions of SCO behavior are carried out using *ab initio* methods such as density functional theory (DFT), but predictions are highly sensitive to the choice of density functional approximation (DFA) from a wide range of available functionals. DFT[43] is widely employed for its relatively modest cost[44-46] but suffers from self-interaction error or delocalization error[47-50] and static correlation error.[51,52] Prior work[39] has demonstrated the barriers to high-throughput screening of SCO complexes with DFT, highlighting the challenges of identifying best-performing functionals. For example, while hybrid functionals and DFT+U make suitable predictions of spin splitting energies, the former are computationally expensive and the latter

2

makes structure and property predictions worse.[39] Prior studies with DFT found B3LYP[53], B3LYP* (i.e., B3LYP with a Hartree–Fock (HF) admixture (a_{HF}) of 0.15)[54,55], TPSSh[56-58], and B2PLYP[59,60] to predict differences in HS and LS states of Fe(II) complexes accurately. Given that these studies are mostly small in scale [61,62] and disagree on what functionals best predict SCO behavior, we recently studied 95 Fe(II) SCO complexes in a data set we curated called SCO-95[40] with over 28 DFAs to determine which functionals make the best predictions of SCO behavior on a larger data set. Although we identified B3LYP (a_{HF} = 0.10), TPSSh, and M06-L[63] to accurately predict the spin splitting Gibbs free energies, we showed they fail to predict the experimental $T_{1/2}$ values we curated from the literature accurately.

Machine learning (ML) has emerged as a powerful tool to complement *ab initio* calculations and accelerate chemical discovery, especially with ML models trained on large sets of experimental data showing comparable accuracy to results from DFT. ML models have found applications in orbital-free DFT,[64,65] accelerating molecular dynamics simulations,[66-68] heterogeneous catalyst design,[69-73] materials discovery,[74-77] force fields,[78-80] potential energy surface representations,[81-85] and many-body expansions.[86,87] ML models have also been used extensively to predict band gaps,[88-90] excited state properties,[91-93] redox potentials,[94,95] electron[96,97] and spin densities,[98-101] and the spin splitting energies[102] highly relevant to predicting SCO behavior. Prior studies[103,104] have also leveraged ML to describe magnetism in materials, which is particularly challenging due to its strong dependence on local environments. One approach[103] employed spin-dependent atom-centered symmetry functions as a type of descriptor for a high-dimensional neural network potential while another[104] built a Euclidean equivariant neural network that preserved the crystallographic symmetry.

Highly relevant to SCO prediction, ML models have been trained to predict more

challenging properties such as the spin states of transition metal complexes (TMCs). Prior studies[41,42,105] from our group used different ML approaches to predict SCO behavior. Through a combination of genetic algorithm and artificial neural networks (ANNs) trained on density functionals with different amounts of HF exchange[102], SCO behavior was predicted through evaluations of ML-predicted[102] spin splitting energies.[105] Another study[41] from our group trained ANNs informed by 23 DFAs to predict SCO behavior through accurate predictions of spin splitting energies. Besides predicting SCO behavior by predictions of spin splitting energies, a study[42] from our group demonstrated the utility of ANNs trained on hybrid DFT by data-mining the literature for SCO complexes by correctly assigning almost all spin states in a set of 46 Fe(II) SCO complexes. Other approaches to predict spin state ordering have used interpretable linear models[106] or neural networks trained using only the local structure around the TM centers.[107]

While ML has been previously leveraged to predict SCO behavior through predictions of spin splitting energies or structural differences between spin states, in this study we use ML models to make predictions of transition temperatures of SCO complexes from the previously curated SCO-95 data set.[40] We train interpretable ML models, i.e., random forest (RF) on a full feature set as well as RF or kernel ridge regression (KRR) on a feature sets selected by RF-ranked recursive feature addition (RF-RFA), on a set of 76 SCO complexes for which experimental $T_{1/2}$ values are available, and we show that these models perform as well or better than the previously-identified best-performing DFAs at predicting experimental transition temperatures. We perform feature selection to identify the most important properties for predicting $T_{1/2}$ values, showing that non-local features are essential to distinguishing the behavior of known SCOs. We also make predictions of $T_{1/2}$ values for a set of 18 SCO complexes for which experimental $T_{1/2}$ values are not reported but can be inferred based on experimental conditions, and, despite the small training

4

set size, we show ML models to outperform the best-performing DFT functionals on this task.

2. Computational Details.

2a. Feature set.

We use a series of revised autocorrelations[94,108] (RACs) as descriptors for all our machine learning (ML) models as prior work[41,95,108-110] demonstrated RACs to be predictive features for transition metal complex (TMC) properties such as ionization potential, electron affinity, redox potential, and spin-splitting energy. Autocorrelations (ACs) are compact descriptors with $d+1$ dimensions per physical property encoded at a maximum depth d, which is the maximum bond-wise path between atoms. These descriptors depend only on connectivity and do not require structural information such as Cartesian or internal coordinates. The properties we employ are five atom-wise heuristic properties on the 2-dimensional molecular graph: Pauling electronegativity (χ); topology (T), which is the coordination number of an atom; nuclear charge (Z); covalent radius (S); and identity (I), which is 1 for any atom. RACs are variants of graph autocorrelations[111-114] that include both sums of products in standard ACs as well as differences, with distinct scopes from ACs, forming a feature set with metal-centric, coordinating atom-centric, and whole-complex descriptors. A standard AC is evaluated over all atoms in a molecule that are d bonds apart:

$$P_d = \sum_i^{Nat} \sum_j^{Nat} P_i P_j \delta (d_{ij}, d) \tag{1}$$

where P_i and P_j are the specific properties of the ith and j^{th} atoms, respectively, δ is the Kronecker delta, and d_{ij} is the number of bonds separating these two atoms. A RAC can have a "start" in the summation, which constrains the atoms that correspond to the summation starts with i, e.g., the metal, from which we can branch out to generate RACs while "scope" dictates the atoms that are permissible as the ends of these branches, e.g., axial ligands, in the summation starting with atom

5

j. The start definition includes RACs that are metal-centered (mc) (i.e., the metal is the start atom), ligand-centered (lc) which are centered on the coordination atoms of ligand (i.e., the ligand coordinating atoms are the start atoms), or over the full molecule (f). The scope definition includes RACs that span to axial (ax) ligands, equatorial (eq) ligands, or all ligands and the metal. This results in six types of RAC start/scope definitions: f/all, f/ax, f/eq, mc/all, lc/ax, and lc/eq. Each of the five atomic property product RACs (eq. 1) have $6d+6$ associated RACs (taking into account the six start/scope definitions), resulting in a total of $30d+30$ product RACs. Difference RACs, which are defined as

$$P'_d = \sum_{i \in \text{start}} \sum_{j \in \text{scope}} (P_i - P_j)\, \delta\, (d_{ij}, d)\, , \tag{2}$$

can be computed non-trivially only for mc and lc RACs for $d > 0$, and only if the atomic property being considered is not I. Difference RACs are therefore evaluated over four atomic properties with three start/scope definitions, resulting in $12d$ difference RACs. In total, the product and difference RACs sum to $42d+30$ theoretical RAC features.[94,108]

As reported in prior work,[94] the typical cutoff of three for the maximum bond depth results in a total of 156 possible RACs. Because we study mononuclear octahedral TMCs in this work, we exclude five constant features corresponding to connectivity around the metal center (e.g., metal coordination number), reducing our feature set to 151 RACs. All the TMCs in our data set have the same metal, i.e., Fe, resulting in three additional constant mc-descriptors: $^{\text{mc}}_{\text{all}}\chi_0$, $^{\text{mc}}_{\text{all}}Z_0$, and $^{\text{mc}}_{\text{all}}S_0$, corresponding to zero-depth RACs with mc/all start/scope definition, and properties of electronegativity, nuclear charge, and covalent radius. Discarding these descriptors leads to a set of 148 RACs. In the original work,[94] four additional descriptors are added to the set of 151 RACs, leading to the RAC-155 feature set. These additional descriptors are the oxidation state, spin state,

6

Hartree–Fock exchange fraction (a_{HF}) in the density functional, and ligand denticity. However, in our SCO-95 data set, all the complexes have the same oxidation state, i.e., Fe(II), and the same spin state, e.g., they are all in either a high-spin quintet or a low-spin singlet state. We also do not study TMC properties as a function of a_{HF} in this work since we obtain all data from experiments. Thus, we do not include these three descriptors (oxidation state, spin state, and a_{HF}) to our set of 148 RACs. However, we do add axial and equatorial ligand denticity descriptors to our feature set to arrive at a final total of 150 features.

2b. Machine learning models and feature selection.

We train three ML models to independently predict transition temperatures ($T_{1/2}$ values) of spin crossover (SCO) complexes: random forest[115] (RF) with a full feature set, RF with features from random-forest-ranked recursive feature addition (RF-RFA), and a kernel ridge regression (KRR) model with features from RF-RFA following the protocol from prior studies.[108,116] In this work, we used 1000 trees to train the RF and RF-RFA models using sklearn[117] v0.24.2 for a 80%/20% train/test split. Additionally, we trained 1000 RF models by changing the random seed and obtained an average of performance metrics for a given train/test split. We pre-process the features using Z-normalization where each feature is normalized to a zero mean and unit variance over the train and test data. Feature selection reduces the dimensionality of the original representation of the data set by eliminating uninformative features, and this process can lead to improved out-of-sample performance of RF-RFA and RF-RFA KRR models.[94,108,118] Feature selection in RF-RFA models is carried out by first assessing model performance when each descriptor is randomly permuted[119], thus yielding an importance score for each descriptor. These descriptors are then provisionally added in order of their importance to the final feature set, which starts with 10 most important features. Following the procedure from prior work,[94] the RF-RFA

7

procedure only permanently includes a descriptor in the final feature set if its inclusion improves model test set performance (coefficient of determination) by at least 1%. If a descriptor is permanently included, the next feature that is considered is provisionally added to an updated version of the final feature set.

In kernel-based methods, i.e., as in our RF-RFA KRR model, inputs are nonlinearly transformed into a higher-dimensional space using the so-called kernel trick. In our KRR models, we focus on tuning two adjustable hyperparameters: the regularization coefficient and kernel width. For RF-RFA KRR models, we accelerated selection of these hyperparameters using the Bayesian optimization Python library Hyperopt[120] v0.2.3. We carried out hyperparameter selection with 200 evaluations on a range of hyperparameters using a random 80/20% train/validation split of the training subset of the original 80/20% train/test split. As in prior work,[41,108,116] recursive feature addition was carried out on random-forest-ranked features (i.e., RF-RFA) to obtain a feature set that gives the best-performing KRR model with the lowest mean absolute error. At each step of the recursive feature addition, a KRR model is trained with an additional descriptor included, and the descriptor is kept only if it improves model performance. All KRR models were implemented in scikit-learn[117] v0.24.2 with a radial basis function kernel.

2c. Data set and density functional theory (DFT) calculations.

As detailed in prior work,[40] we curated the SCO-95 data set of 95 octahedral, mononuclear Fe(II) spin crossover (SCO) complexes from the Cambridge Structural Database.[121] Previously,[40] we both curated experimental transition temperatures ($T_{1/2}$ values) along with DFT-predicted values, which corresponds to the temperature at which SCO is observed for these complexes (Figure 1). For the predictions, we used DFT with 28 density functional approximations (DFAs)

8

across the various rungs of "Jacob's ladder"[122] along with free energy corrections obtained at a single temperature (T = 300 K) and functional, i.e., modified B3LYP (modB3LYP) with Hartree–Fock (HF) exchange (a_{HF}) of 0.10. In the present work, we report the previously computed $T_{1/2}$ values for the three best-performing functionals from the original 28 DFA set, modB3LYP (a_{HF} = 0.10), M06-L, and TPSSh. Of the 95 complexes in our data set, experimental transition temperatures were reported for 76 complexes, while the remaining 19 complexes exhibit a two-step SCO behavior or a single-step SCO without an experimentally reported $T_{1/2}$ value (Figure 1). Experimental $T_{1/2}$ values mostly range from 100 K to 375 K for the complexes in SCO-95 data set,[40] with two outliers (refcodes: EXARAY[123] and ESOSOW[124]) closer to 450 K (Figure 1 and Supporting Information Figure S1). In this study, we train ML models on $T_{1/2}$ values of all 76 complexes and also on 74 complexes after removing the two outliers to understand how their exclusion affects model performance. We then use the trained ML models to predict transition temperatures for the remaining 19 complexes for which experimental $T_{1/2}$ values are not reported. We compare the ML-predicted values to the estimated experimental $T_{1/2}$ obtained as the average of low-temperature (low-T) and high-temperature (high-T) of crystallization. We also compare the estimated $T_{1/2}$ values of the 19 complexes to those from DFT calculations.
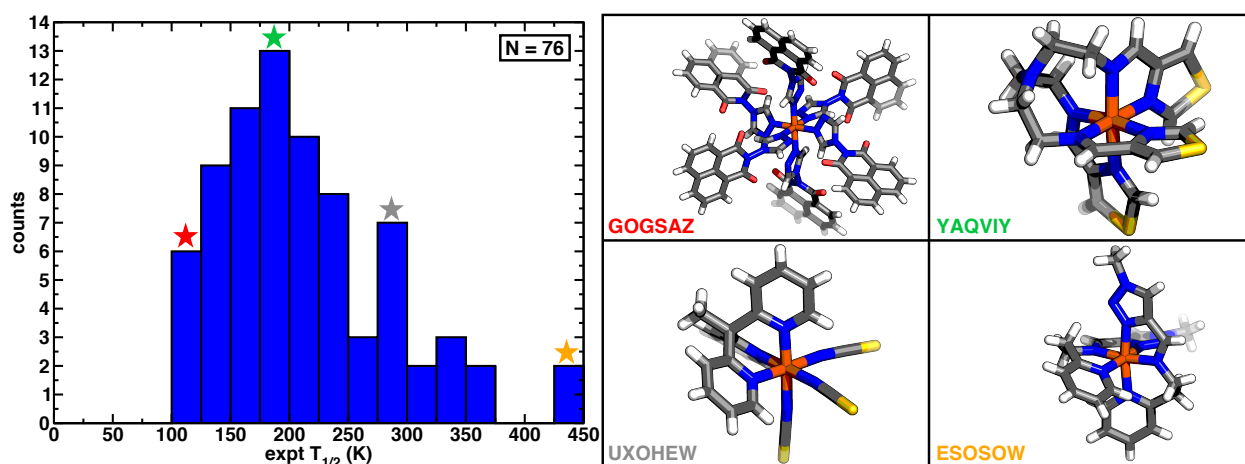

Figure 1. (Left) Histogram of experimentally (expt) reported transition temperatures ($T_{1/2}$ in K) for N = 76 complexes. Representative low-temperature, low-spin Fe(II) SCO complexes

9

corresponding to a wide range of $T_{1/2}$ values are shown as insets. Complexes with refcodes GOGSAZ,[125] YAQVIY,[126] UXOHEW,[127] and ESOSOW[124] exhibit SCO behavior at $T_{1/2}$ values of 114 K, 190 K, 290 K, and 445 K, respectively. The bin width of the histogram is 25 K, and bins containing inset structures are indicated with color-matched stars. Hydrogen, carbon, nitrogen, oxygen, sulfur, and iron are shown in white, gray, blue, red, yellow, and brown, respectively.

3. Results and Discussion.

3a. $T_{1/2}$ predictions from ML models vs DFT.

In prior work,[40] we computed Gibbs free energy spin splitting energies ($\Delta G_{\text{H-L}}$) and transition temperatures ($T_{1/2}$ values) with 28 density functional approximations (DFAs) for Fe(II) spin crossover (SCO) complexes in the SCO-95 data set. From this initial set, three functionals, i.e., M06-L, TPSSh, and modB3LYP (a_{HF} =0.10), performed best by predicting $\Delta G_{\text{H-L}}$ values that would be suggestive of experimental spin crossover behavior. Although these functionals qualitatively predicted SCO behavior, they still failed to accurately predict $T_{1/2}$ values. Instead, they predict an unphysically wide range of $T_{1/2}$ values (-200 K to 1200 K), in contrast to the 100 K to 450 K range of experimentally reported $T_{1/2}$ values for 76 SCO complexes in the SCO-95 data set. In this study, we trained machine learning (ML) models on $T_{1/2}$ values to find out if ML models can make better predictions of experimental $T_{1/2}$ values.

We trained three machine learning (ML) models, namely, RF with a full feature set, RF with an RF-RFA selected feature set, and KRR with an RF-RFA selected feature set, on experimentally reported $T_{1/2}$ values in the SCO-95 data set and made predictions on a set-aside test set. RF and RF-RFA RF models trained on $T_{1/2}$ values of 59 SCO complexes outperform the RF-RFA KRR model (Figure 2 and Supporting Information Table S1). Given the small dataset size and difficulty of predicting a narrow range of $T_{1/2}$ values, unsurprisingly none of the models perform particularly well. RF and RF-RFA RF models exhibit smaller mean absolute errors (MAE)

10

of ca. 40 K and show comparable correlation to experimentally reported $T_{1/2}$ values, i.e., Pearson's r of 0.36 and 0.34, and Spearman's ρ of 0.28 and 0.23, respectively, indicating that feature selection does not improve over the standard RF model (Figure 2 and Supporting Information Table S1). Nevertheless, starting RF-RFA feature selection for the RF model with fewer initial features did not improve the imbalance in train-test performance. The MAE of the RF-RFA KRR model is three times as large, and predictions from this model exhibit a poor correlation to experimental $T_{1/2}$ values as quantified by a Pearson's r of -0.10 and a Spearman's ρ of -0.29 (Figure 2 and Supporting Information Table S1). Further examination reveals the presence of an outlier only for the KRR model, i.e., an SCO complex with refcode WIHQIQ,[128] for which RF-RFA KRR severely overpredicts $T_{1/2}$, predicting a $T_{1/2}$ value of 723 K compared to the experimental $T_{1/2}$ value of 220 K (Figure 2). This complex is distinct from the majority of the complexes in the data set, which predominantly contain six Fe–N bonds, since it contains six longer Fe–S bonds (Figure 2). The removal of this complex from the test set improves the performance of the RF-RFA KRR model, reducing the MAE to 46 K and improving correlation to experimental values with a Pearson's r of 0.24 (Supporting Information Table S1 and Figure S2). The large effect of the outlier on RF-RFA KRR performance shows that when the ligand coordinating atoms of a complex differ from the nitrogen atoms present in the majority of the data set, RF-RFA KRR struggles to make reasonable predictions of $T_{1/2}$ values.
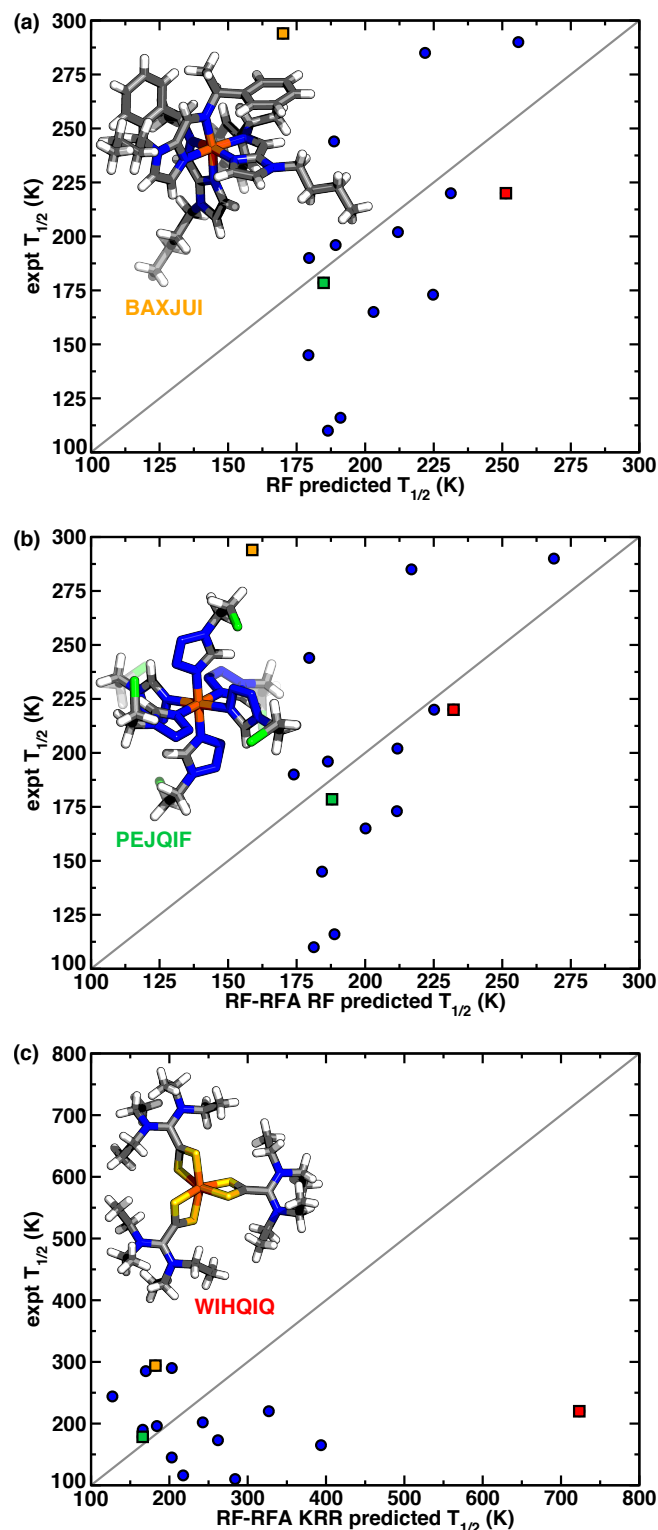
Figure 2. Plots of transition temperatures ($T_{1/2}$ values in K) predicted by (a) RF, (b) RF-RFA RF, and (c) RF-RFA KRR vs experimental (expt) $T_{1/2}$ values of the 15 SCO complexes in the test set. These models were trained over a data set of 59 SCO complexes, with a total of 74 SCO complexes in the training and test sets. Representative structures corresponding to SCO complexes (refcodes: BAXJUI,[129] PEJQIF,[130] and WIHQIQ[128]) highlighted in orange, green, and red squares,

respectively, are shown as insets. Hydrogen, carbon, nitrogen, sulfur, chlorine, and iron are shown in white, gray, blue, yellow, green, and brown, respectively. The parity line is shown in solid gray in   the   plots.

If we include the two high transition temperature compounds that were initially excluded from the data, one each in training and test sets, we see comparable training set performance but worsened test set performance (Supporting Information Table S1 and Figures S3–S5). In particular, inclusion in the test set of one of the outliers with $T_{1/2}$ of 445 K leads to larger MAE values of ca. 85 K for RF or RF-RFA and 130 K for RF-RFA KRR (Supporting Information Table S1 and Figure S5).

Next, we compare DFA-predicted $T_{1/2}$ values and ML-predicted $T_{1/2}$ values on the 15 SCO molecules in the ML test set relative to experimentally reported $T_{1/2}$ values. We find that the ML model predictions of $T_{1/2}$ values have much lower errors in comparison to experimentally reported $T_{1/2}$ values than DFA-predicted $T_{1/2}$ values do (Figures 2 and 3). The DFT MAE on the test set with outliers removed is highest at 512 K for TPSSh and lowest for M06-L at 162 K (Figure 3 and Supporting Information Table S2). Despite this better overall performance of M06-L, the larger spread in values from the modB3LYP ($a_{HF} = 0.10$) and TPSSh functionals leads to them exhibiting a better Pearson's r and Spearman's ρ relative to M06-L, i.e., ca. 0.50 for TPSSh or B3LYP vs 0.25 for M06-L (Figure 3 and Supporting Information Table S2). Further examination reveals that modB3LYP ($a_{HF} = 0.10$) and TPSSh predictions have extreme outliers (refcodes: OSABOB[131] and UXOHEW[127]) resulting in very large MAE values (Figure 3). While the DFA-predicted $T_{1/2}$ values show MAE of up to ca. 500 K vs an MAE of 40 K observed for best-performing ML models, their Pearson's r and Spearman's ρ are modestly better than the ML models (Figures 2 and 3 and

13

Supporting Information Tables S1–S2). The DFA predictions on the larger training sets of ca. 60 complexes are comparable to their predictions on the smaller test sets of 15 complexes, meaning that the choice of the test set complexes did not strongly affect DFA assessment (Figure 3 and Supporting Information Table S2 and Figure S6). Overall, the RF and RF-RFA RF ML models have mixed performance compared to DFAs (i.e., lower MAE, comparable Pearson's r values, and slightly worse Spearman's ρ values), but the clear advantage is in the dramatically lower cost for applying our ML models in comparison to the full DFT evaluation.
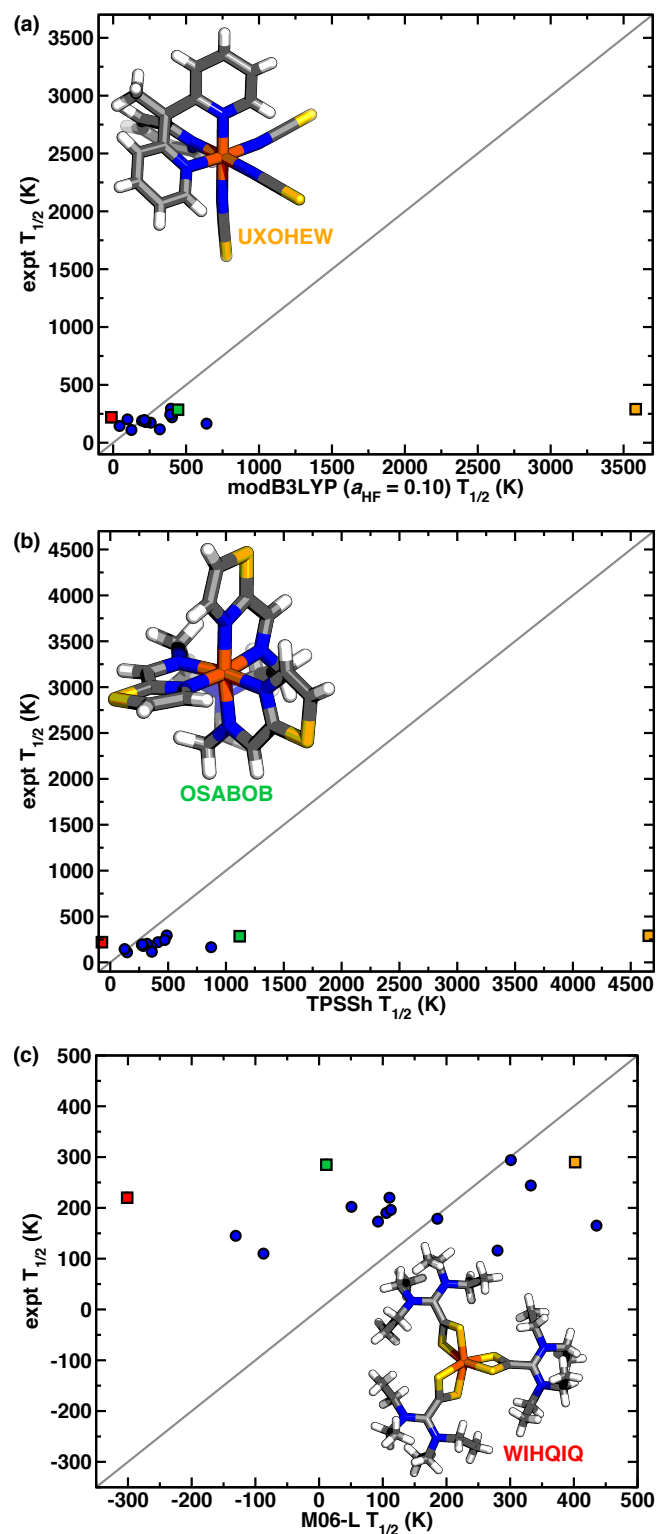
14

Figure 3. Plots of transition temperatures ($T_{1/2}$ values in K) predicted by (a) modB3LYP (a_{HF} = 0.10), (b) TPSSh, and (c) M06-L vs experimental (expt) $T_{1/2}$ values of the 15 SCO complexes in the test set. Representative structures corresponding to SCO complexes (refcodes: UXOHEW,[127] OSABOB,[131] and WIHQIQ[128]) highlighted in orange, green, and red squares, respectively, are

shown as insets. Hydrogen, carbon, nitrogen, sulfur, and iron are shown in white, gray, blue, yellow, and brown, respectively. The parity line is shown in solid gray in the plots.

3b. $T_{1/2}$ predictions of ML models on a blind set of SCO complexes.

We now aimed to test our trained ML models on SCO complexes from the SCO-95 data set where experimental $T_{1/2}$ values were not available. To validate our method of estimation, we compared[40] estimated $T_{1/2}$ values as an average of low- and high-temperatures (low-T and high-T) of crystallization and found excellent agreement for this set of 74 SCO complexes, with a high Pearson's r of 0.93 and Spearman's ρ of 0.89 (Supporting Information Figure S7). Thus, over the remaining set of 19 SCO complexes from the SCO-95 data set where experimental $T_{1/2}$ values are not reported, we were able to obtain estimated $T_{1/2}$ values for 18 complexes. We could not obtain estimated $T_{1/2}$ for one complex (refcode: JOTQAN[132]) because the high-temperature of crystallization for this complex was not reported. These 18 SCO complexes all have Fe–N bonds and ligands that contain hydrogen, carbon, and nitrogen, with some complexes additionally containing boron, oxygen, sulfur, and bromine (Supporting Information Figures S8–S9). Of these 18 complexes, 8 of them exhibit two-step SCO behavior while the rest show gradual single-step SCO behavior (Supporting Information Figures S8–S9).

We compare estimated experimental $T_{1/2}$ values to the $T_{1/2}$ predictions of the trained RF, RF-RFA RF, and RF-RFA KRR models on this blind test set of 18 SCO complexes for which experimental $T_{1/2}$ values are not reported. $T_{1/2}$ values predicted by the RF-RFA RF model trained on 59 SCO complexes (total of 74 complexes in training and test sets) show moderate correlation to estimated $T_{1/2}$ values for the blind set, with a Pearson's r of 0.25, Spearman's ρ of 0.28, and MAE of 44 K (Figure 4 and Supporting Information Table S3). This performance is roughly

16

comparable to that on the original test set (i.e., test: MAE 40.5 K, Pearson's r = 0.34 and Spearman's ρ = 0.23, see Supporting Information Table S1). We observe that the RF-RFA RF model performs only slightly better than the RF model, and both these models outperform the RF-RFA KRR model (Figure 4 and Supporting Information Table S3). The predictions from the KRR model show no correlation with estimated $T_{1/2}$ values and have a large MAE of 104 K (Figure 4 and Supporting Information Table S3). Consistent with prior observations, all ML models trained on the set of 61 SCO complexes, which includes an outlier with a large $T_{1/2}$ value of 445 K, perform worse on the blind set of 18 SCO complexes (Supporting Information Table S3 and Figure S10).
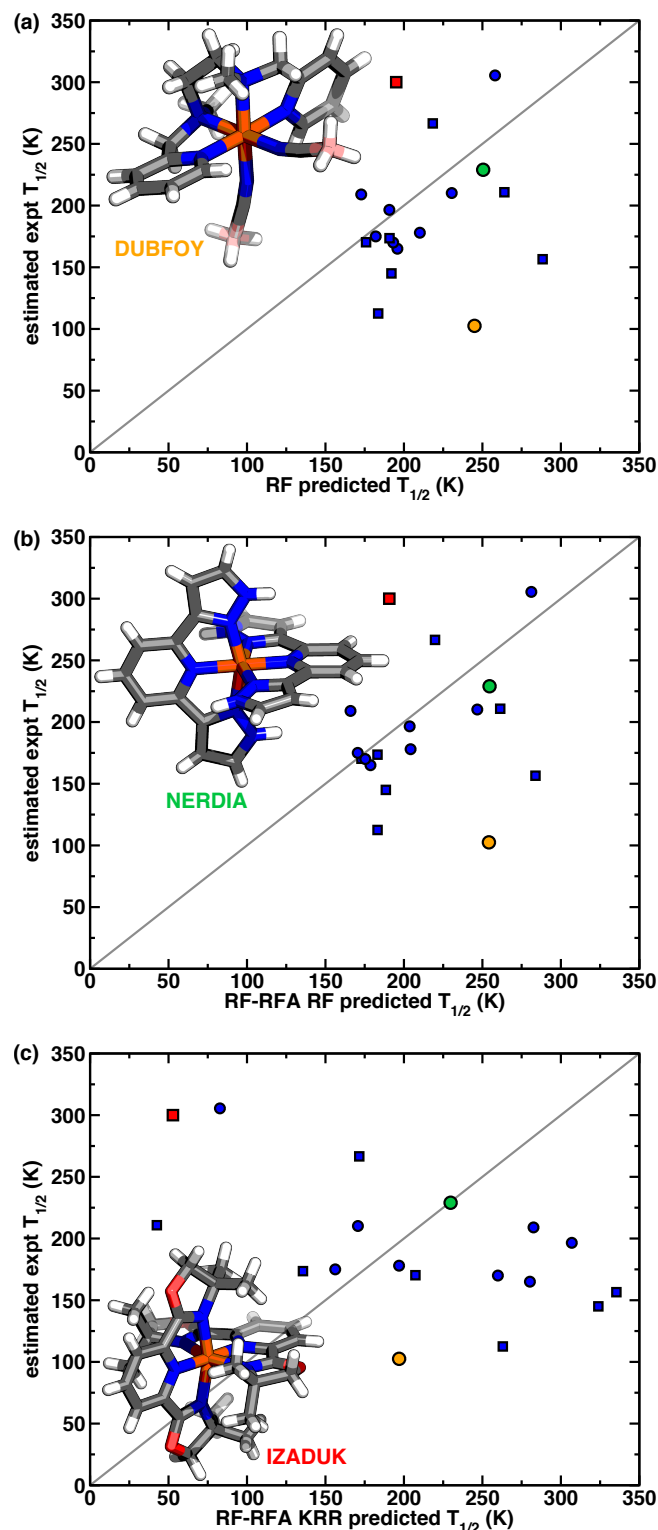
17

Figure 4. Plots of transition temperatures (T$_{1/2}$ values in K) predicted by the trained ML models: (a) RF, (b) RF-RFA RF, and (c) RF-RFA KRR T$_{1/2}$ predictions vs estimated experimental (expt) T$_{1/2}$ values of the 18 SCO complexes in the blind set. These models were trained on the 59 SCO complexes in the training set with a total of 74 SCO complexes across both training and test sets. Data points of SCO complexes that exhibit single-step and two-step SCO behavior are represented

18

with circles and squares, respectively. Representative structures corresponding to SCO complexes (refcodes: DUBFOY,[133] NERDIA,[134] and IZADUK[31]) are shown as insets, and their data points are highlighted with orange circle, green circle, and red square, respectively. Hydrogen, boron, carbon, nitrogen, oxygen, and iron are shown in white, pink, gray, blue, red, and brown, respectively. The parity line is shown in solid gray in the plots.

One of the reasons that these 18 complexes lack reported $T_{1/2}$ values is that they undergo two-step SCO. We expect ML-predicted $T_{1/2}$ values to be in agreement with estimated $T_{1/2}$ values only for complexes that show single-step SCO behavior because the models were trained on such complexes. Indeed, in the blind set of 18 complexes, we observe that for some of the complexes that exhibit two-step SCO behavior, ML-predicted $T_{1/2}$ values are significantly different from the estimated $T_{1/2}$ values (Figure 4 and Supporting Information Figure S8 and Table S4). For example, ML models considerably underestimate the $T_{1/2}$ of an SCO complex (refcode: IZADUK[31]) that exhibits two-step SCO behavior, i.e., ML-predicted $T_{1/2}$ of ca. 190 K vs estimated $T_{1/2}$ of 300 K (Figure 4 and Supporting Information Table S4). However, for a smaller test set of 10 SCO complexes obtained after removing the complexes with two-step SCO behavior, RF-RFA RF and RF models show improved correlation to estimated $T_{1/2}$ values with a Pearson's r of 0.40 and 0.32, respectively (Supporting Information Table S5). We also observe that ML models strongly overestimate the $T_{1/2}$ of a blind set complex (refcode: DUBFOY[133]) that contains boron atoms, i.e., ML-predicted $T_{1/2}$ of ca. 250 K vs estimated $T_{1/2}$ of 102 K (Figure 4). Further examination reveals that all the complexes in the training set that contain boron atoms show large $T_{1/2}$ values (>180 K) which likely causes the larger ML-predicted $T_{1/2}$ of DUBFOY. Excluding this complex leads to very strong correlation of RF and RF-RFA RF-predicted $T_{1/2}$ values to estimated $T_{1/2}$ values over the resultant 9 SCO complex set, with a Pearson's r of 0.74 and 0.82, and Spearman's ρ of 0.55 and 0.67, respectively (Supporting Information Table S6 and Figure S11).

Finally, we compare ML $T_{1/2}$ predictions on the blind set to DFA $T_{1/2}$ predictions from the three best-performing functionals, i.e., modB3LYP (a_{HF} = 0.10), TPSSh, and M06-L (Figures 4 and 5). DFA $T_{1/2}$ predictions show little correlation with estimated $T_{1/2}$ values for the set of 18 SCO complexes as quantified by a poor Pearson's *r* of 0.03-0.08 and very large MAEs of up to 400 K (Figure 5 and Supporting Information Table S3). Consistent with prior observations on the test set performance, M06-L performs slightly better than the other two DFAs, with a relatively small MAE of 179 K (Figure 5 and Supporting Information Table S3). However, we find that all three DFAs consistently fail at predicting the $T_{1/2}$ of a complex (refcode: ECODIM[135]) which shows two-step SCO behavior, i.e., strongly negative DFA-predicted $T_{1/2}$ values vs estimated $T_{1/2}$ of 174 K (Figure 5). While ML models show improved performance on a smaller set of 9 SCO complexes after removing those with two-step SCO behavior and with boron atoms, the DFA $T_{1/2}$ predictions show no correlation to estimated $T_{1/2}$ values even over the smaller set (Supporting Information Tables S5–S6 and Figure S12). Overall, RF and RF-RFA RF models outperform the DFA approach in SCO complex transition temperature prediction across the SCO-95 data set, as confirmed through predictions on the set of SCO complexes for which experimental $T_{1/2}$ values are not reported.
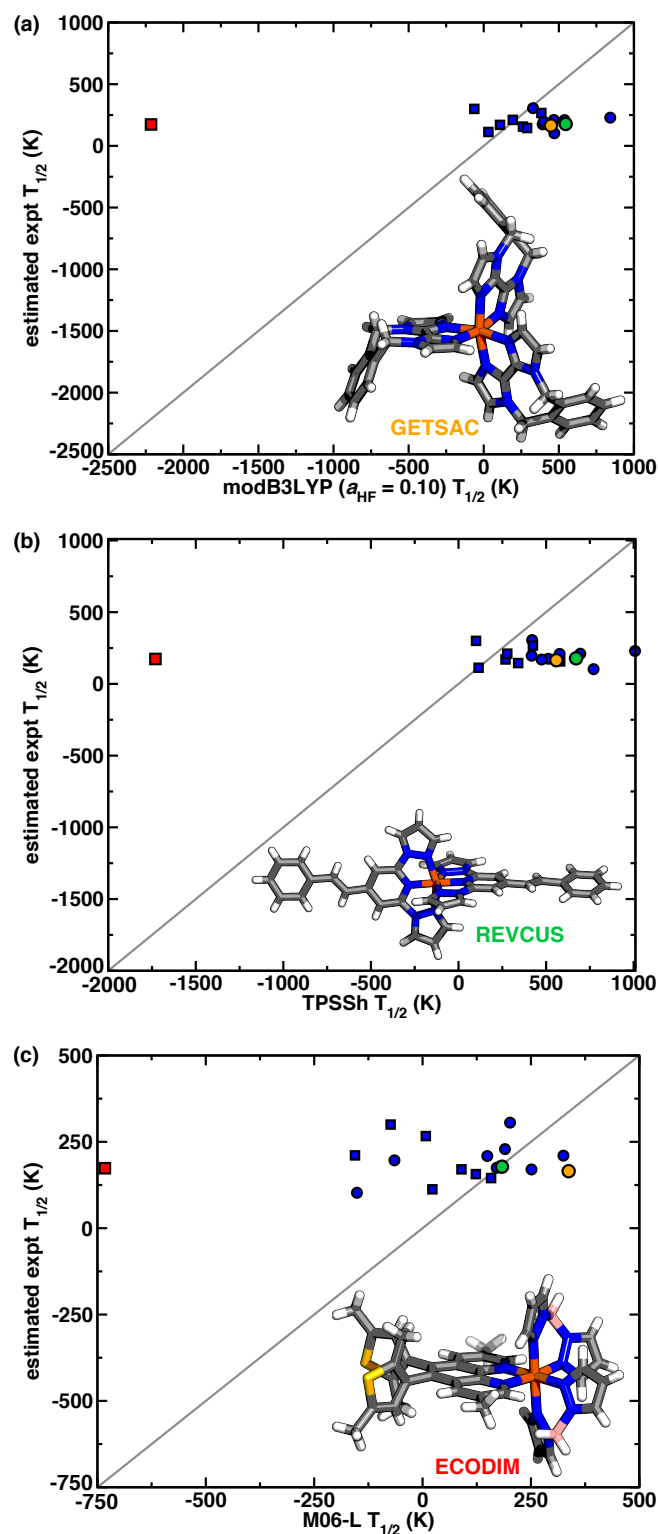
Figure 5. Plots of transition temperatures ($T_{1/2}$ values in K) predicted by the DFAs: (a) modB3LYP (a_{HF} = 0.10), (b) TPSSh, and (c) M06-L $T_{1/2}$ predictions vs estimated experimental (expt) $T_{1/2}$ values of the 18 SCO complexes in the blind set. Data points of SCO complexes that exhibit single-step and two-step SCO behavior are represented with circles and squares, respectively.

21

Representative structures corresponding to SCO complexes (refcodes: GETSAC,[136] REVCUS,[137] and ECODIM[135]) are shown as insets, and their data points are highlighted with orange circle, green circle, and red square, respectively. Hydrogen, boron, carbon, nitrogen, sulfur, and iron are shown in white, pink, gray, blue, yellow, and brown, respectively. The parity line is shown in solid gray in the plots.

3c. Important features in making $T_{1/2}$ predictions.

The large number of RACs, i.e., 150 features (see Sec 2), relative to the number of complexes in our dataset makes it essential to identify the most important features to train transferable models. Identification of these features also provides insight in terms of their graph-based proximity to the metal center as well as their electronic and geometric nature. The identification of these important features can be used to reveal design principles for the discovery of new SCO materials.

We perform feature selection using RF-RFA with RF and KRR models and observe a better performance of the RF-RFA RF model than the KRR model (see Sec 3b). We identify the 14 most important RAC features using an RF-RFA RF model by training it on $T_{1/2}$ values of 74 SCO complexes obtained after removing two outliers (refcodes: ESOSOW[124] and EXARAY[123]) from the set of 76 SCO complexes with experimentally reported $T_{1/2}$ values (Figure 6 and Supporting Information Table S7). As in prior work[94], we group features as metal-local and metal-distal, where metal-local features correspond to those within two bond paths of the metal, i.e., the metal, its first and second coordination spheres, while metal-distal features correspond to the third coordination sphere and the more distant global features (Figure 6). Analysis of model feature importance reveals that all selected features are metal-distal in nature and identifies global features to be more important than the more metal-proximal second and third coordination sphere features for predicting $T_{1/2}$ values, despite an expectation that the variation of the second and third coordination sphere could drive significant changes in spin state energetics (Figure 6). We also find that

22

electronic features, i.e., nuclear charge (Z) and Pauling electronegativity (χ), play a slightly more important role (i.e., over 55% of selected features are electronic in nature) than geometric features, i.e., topology (T), covalent radius (S), and identity (I), although the prediction of this property has a greater contribution of geometric effects than observed for the prediction of DFT-calculated spin states of a larger set of molecules[94] (Figure 6). To ensure robustness in our observations to the method of feature selection, we compare to RF-RFA KRR models trained to obtain the most important features in the prediction of $T_{1/2}$ values where 25 features are identified (Figure 6 and Supporting Information Table S7). Analysis of the selected RF-RFA KRR features reveals that ca. 65% of RF-RFA RF-selected features are present in the KRR-selected feature set (Supporting Information Table S7). While RF-RFA KRR-selected features also identify global features to be most important, a small fraction of metal-proximal second coordination sphere features are also selected (Figure 6). Additionally, we observe comparable numbers of electronic and geometric features (52% vs 48%) in this feature set, confirming the robustness of our selected features to the ML model (Figure 6).
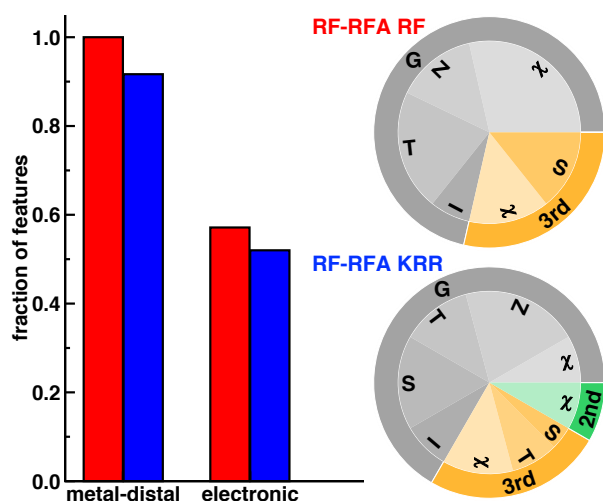

Figure 6. (Left) Plot showing the fraction of metal-distal features and the fraction of electronic features selected by RF-RFA RF (red) and RF-RFA KRR (blue) models for the prediction of transition temperatures of 74 complexes in the SCO-95 data set. (Right) Pie charts of (top) the RF-RFA RF and (bottom) RF-RFA KRR-selected features from the initial set of 150 features. Features

23

are grouped by the most metal-distal atoms: more distant, global features in gray, third coordination sphere features in orange, and second coordination sphere features in green. Within each connectivity distance category, the property (i.e., χ, S, T, Z, or I) is indicated. Following our previous work,[108,116] we have categorized χ and Z as electronic features, with all remaining features categorized as geometric.

To analyze how the models would perform if we included the outliers with higher transition temperatures, we also carried out RF-RFA with RF and KRR on all 76 complexes from the SCO-95 data set. We observe that around 20 important features are selected by both models (Supporting Information Table S7 and Figure S13). While both models identify global features to be most important which is consistent with our observations from the set of 74 complexes, electronic features play a much more important role than geometric features, i.e., 64% vs 36% (Supporting Information Table S7 and Figure S13). Although all the results discussed correspond to a particular random split of the data, the results averaged from up to 1000 random splits are also found to largely be in agreement (Supporting Information Figure S14). These findings about feature importance can guide future SCO material design, since tuning the metal-distal global properties for a variety of Fe(II) complexes is expected to tune $T_{1/2}$.

4. Conclusions.

In summary, we trained three ML models to predict transition temperatures of SCO complexes in the previously[40] curated SCO-95 data set. We performed feature selection using RF-RFA to identify the most important features to train transferable models. Of the three ML models we studied, the RF and RF-RFA RF models performed comparably with moderate correlation to experimental $T_{1/2}$ values. From feature selection, we identified a strong emphasis on global features rather than the more metal-proximal second and third coordination sphere features for

predicting $T_{1/2}$ values. We also found that electronic and geometric features contributed nearly equally to predicting SCO behavior. These observations emphasized exploring metal-distal contributions to molecules to fine-tune Fe(II) SCO design.

We compared the ML predictions to $T_{1/2}$ predictions of DFAs for three previously identified[40] best-performing DFAs, i.e., modB3LYP (a_{HF} = 0.10), TPSSh, and M06-L. These functionals predicted SCO behavior of most complexes by correctly predicting their free energies of spin transition but with poor predictions of $T_{1/2}$ values. We observed that the DFA $T_{1/2}$ predictions had much higher MAEs than the ML models albeit with relatively comparable Pearson's r correlation between DFT and experimental $T_{1/2}$ values as compared to that between ML $T_{1/2}$ predictions and experimental $T_{1/2}$ values. To further validate the ML model approach, we studied ML model predictions on the set of 18 SCO complexes for which experimental $T_{1/2}$ values are not reported by estimating their $T_{1/2}$ values from the average of low-T and high-T of crystallization. Upon excluding the SCO complexes that showed two-step SCO behavior and one containing boron, the RF-RFA RF model showed stronger correlation to estimated $T_{1/2}$ values over the resulting set of 9 complexes with a Pearson's r of 0.82. However, DFA-predicted $T_{1/2}$ values had large errors and showed no correlation to estimated $T_{1/2}$ values over the set of 18 SCO complexes nor over the smaller set of 9 SCO complexes which solely exhibit single-step SCO behavior. Overall, our study of ML and DFA $T_{1/2}$ predictions of Fe(II) SCO complexes in the SCO-95 data set highlights that random forest models show reasonable performance comparable to some of the best performing density functionals at much lower computational cost. We expect this performance to improve as larger datasets of experimental SCOs are curated. Alternatively, inclusion of DFT-predicted quantities from best-performing functionals could also be used to increase model performance, albeit at higher computational cost.

ASSOCIATED CONTENT

AUTHOR INFORMATION

Notes

The authors declare no competing financial interest.

Supporting Information. Structures of SCO complexes with larger $T_{1/2}$ values of 445 K; features selected by RF-RFA RF and RF-RFA KRR models; fraction of metal-distal and electronic features selected; fraction of features selected as averaged over 1000 random splits; MAE, Pearson's r, and Spearman's ρ of $T_{1/2}$ predictions by ML models; plot of RF-RFA RF $T_{1/2}$ predictions on test set vs experimental $T_{1/2}$; plots of ML $T_{1/2}$ predictions on training set of 61 SCOs vs experimental $T_{1/2}$; plots of ML $T_{1/2}$ predictions on training set of 59 SCOs vs experimental $T_{1/2}$; plots of ML $T_{1/2}$ predictions on test set vs experimental $T_{1/2}$; MAE, Pearson's r, and Spearman's ρ of $T_{1/2}$ predictions by DFAs; plots of DFA $T_{1/2}$ predictions on training set vs experimental $T_{1/2}$; plot of estimated $T_{1/2}$ vs experimental $T_{1/2}$; structures of 8 SCO complexes that exhibit two-step SCO behavior; structures of 10 SCO complexes that exhibit single-step SCO behavior; MAE, Pearson's r, and Spearman's ρ of ML and DFA $T_{1/2}$ of blind set; plots of ML $T_{1/2}$ predictions on blind set of 18 SCOs vs estimated $T_{1/2}$; ML $T_{1/2}$ predictions of SCO complexes that exhibit two-step SCO behavior; MAE, Pearson's r, and Spearman's ρ of ML $T_{1/2}$ of blind set of 10 SCOs; MAE, Pearson's r, and Spearman's ρ of ML $T_{1/2}$ of blind set of 9 SCOs; plots of ML $T_{1/2}$ predictions on blind set of 9 SCOs vs estimated $T_{1/2}$; plots of DFA $T_{1/2}$ predictions on blind set of 9 SCOs vs estimated $T_{1/2}$ (PDF)

Jupyter notebooks and python codes detailing the ML methods used; CSV files with Fe(II) SCO complexes from the SCO-95 data set along with the corresponding RACs, experimentally reported and estimated transition temperatures when available (ZIP)

This material is available free of charge via the Internet at http://pubs.acs.org.

ACKNOWLEDGMENT

References

(1)   Gütlich, P.; Goodwin, H. A. Spin Crossover in Transition Metal Compounds I-Iii. **2004**.

(2)   Konig, E.; Ritter, G.; Kulshreshtha, S. K. The Nature of Spin-State Transitions in Solid Complexes of Iron(Ii) and the Interpretation of Some Associated Phenomena. *Chem. Rev.* **1985,** *85*, 219-234.

(3)   Takahashi, K. Spin-Crossover Complexes. *Inorganics* **2018,** *6*, 32.

(4)   Real, J. A.; Gaspar, A. B.; Munoz, M. C. Thermal, Pressure and Light Switchable Spin-Crossover Materials. *Dalton. Trans.* **2005**, 2062-2079.

(5)   Halcrow, M. A. Spin-Crossover Materials: Properties and Applications. . *John Wiley & Sons, Ltd., Hoboken/New Jersey* **2013**.

(6)   Gutlich, P.; Hauser, A.; Spiering, H. Thermal and Optical Switching of Iron(Ii) Complexes. *Angew Chem Int Edit* **1994,** *33*, 2024-2054.

(7)   Homenya, P.; Heyer, L.; Renz, F. Electromagnetic Radiation as a Spin Crossover Stimulus. *Pure Appl. Chem.* **2015,** *87*, 293-300.

(8)   Gaspar, A. B.; Molnar, G.; Rotaru, A.; Shepherd, H. J. Pressure Effect Investigations on Spin-Crossover Coordination Compounds. *C. R. Chim.* **2018,** *21*, 1095-1120.

(9)   Decurtins, S.; Gutlich, P.; Kohler, C. P.; Spiering, H.; Hauser, A. Light-Induced Excited Spin State Trapping in a Transition-Metal Complex - the Hexa-1-Propyltetrazole-Iron (Ii) Tetrafluoroborate Spin-Crossover System. *Chem. Phys. Lett.* **1984,** *105*, 1-4.

(10)   Hauser, A. Light-Induced Spin Crossover and the High-Spin -> Low-Spin Relaxation. *Top. Curr. Chem.* **2004,** *234*, 155-198.

(11)   Naonobu, S.; Shin-ichi, O.; Osamu, S.; Kazuhito, H. One-Shot-Laser-Pulse-Induced Cooperative Charge Transfer Accompanied by Spin Transition in a Co-Fe Prussian Blue Analog at Room Temperature. *Chem. Lett.* **2002,** *31*, 486-487.

(12)   Sousa, C.; Llunell, M.; Domingo, A.; De Graaf, C. Theoretical Evidence for the Direct (Mlct)-M-3-Hs Deactivation in the Light-Induced Spin Crossover of Fe((Ii))-Polypyridyl Complexes. *Phys. Chem. Chem. Phys.* **2018,** *20*, 2351-2355.

(13)   Kahn, O.; Krober, J.; Jay, C. Spin Transition Molecular Materials for Displays and Data Recording. *Adv. Mater.* **1992,** *4*, 718-728.

(14)   Bhandary, S.; Tomczak, J. M.; Valli, A. Designing a Mechanically Driven Spin-Crossover Molecular Switch Via Organic Embedding. *Nanoscale Adv.* **2021,** *3*, 4990-4995.

(15)   Bousseksou, A.; Molnar, G.; Demont, P.; Menegotto, J. Observation of a Thermal Hysteresis Loop in the Dielectric Constant of Spin Crossover Complexes: Towards Molecular Memory Devices. *J. Mater. Chem.* **2003,** *13*, 2069-2071.

(16)   Linares, J.; Codjovi, E.; Garcia, Y. Pressure and Temperature Spin Crossover Sensors with Optical Detection. *Sensors* **2012,** *12*, 4479-4492.

(17)   Letard, J.-F.; Guionneau, P.; Goux-Capes, L. Towards Spin Crossover Applications. *Spin Crossover in Transition Metal Compounds Iii* **2004,** *235*, 221-249.

(18)   Krober, J.; Codjovi, E.; Kahn, O.; Groliere, F.; Jay, C. A Spin Transition System with a Thermal Hysteresis at Room-Temperature. *J. Am. Chem. Soc.* **1993,** *115*, 9810-9811.

(19)   Rudavskyi, A.; Sousa, C.; de Graaf, C.; Havenith, R. W. A.; Broer, R. Computational Approach to the Study of Thermal Spin Crossover Phenomena. *Journal of Chemical Physics* **2014,** *140*, 184318.

(20) Halcrow, M. A. Structure:Function Relationships in Molecular Spin-Crossover Complexes. *Chem. Soc. Rev.* **2011,** *40*, 4119-4142.

(21) Konig, E. Structural-Changes Accompanying Continuous and Discontinuous Spin-State Transitions. *Progress in Inorganic Chemistry* **1987,** *35*, 527-622.

(22) Halcrow, M. A. The Spin-States and Spin-Transitions of Mononuclear Iron(Ii) Complexes of Nitrogen-Donor Ligands. *Polyhedron* **2007,** *26*, 3523-3576.

(23) Murray, K. S. Advances in Polynuclear Iron(Ii), Iron(Iii) and Cobalt(Ii) Spin-Crossover Compounds. *Eur J Inorg Chem* **2008**, 3101-3121.

(24) Ruiz, E. Charge Transport Properties of Spin Crossover Systems. *Phys. Chem. Chem. Phys.* **2014,** *16*, 14-22.

(25) Cirera, J.; Ruiz, E. Computational Modeling of Transition Temperatures in Spin-Crossover Systems. *Comments Inorg. Chem.* **2019,** *39*, 216-241.

(26) Matouzenko, G. S.; Letard, J.-F.; Lecocq, S.; Bousseksou, A.; Capes, L.; Salmon, L.; Perrin, M.; Kahn, O.; Collet, A. Two-Step Spin Crossover in a Mononuclear Compound [Fe(Dpea)(Bim)](Clo4)(2)Center Dot 0.5 H2o[Dpea = (2-Aminoethyl)-Bis(2-Pyridylmethyl)Amine, Bim=2,2-Bisimidazole] - Crystal Structure, Magnetic Properties, Mossbauer Spectroscopy, and Photomagnetic Effects. *Eur J Inorg Chem* **2001**, 2935-2945.

(27) Hang, H.; Fei, B.; Chen, X. Q.; Tong, M. L.; Ksenofontov, V.; Gural'skiy, I. y. A.; Bao, X. Multiple Spin Phases in a Switchable Fe(Ii) Complex: Polymorphism and Symmetry Breaking Effects. *J. Mater. Chem. C* **2018,** *6*, 3352-3361.

(28) Sato, T.; Nishi, K.; Iijima, S.; Kojima, M.; Matsumoto, N. One-Step and Two-Step Spin-Crossover Iron(Ii) Complexes of ((2-Methylimidazol-4-Yl)Methylidene)Histamine. *Inorg. Chem.* **2009,** *48*, 7211-7229.

(29) Herber, R.; Casson, L. M. Light-Induced Excited-Spin-State Trapping - Evidence from Vtftir Measurements. *Inorganic Chemistry* **1986,** *25*, 847-852.

(30) Zilverentant, C. L.; van Albada, G. A.; Bousseksou, A.; Haasnoot, J. G.; Reedijk, J. Infrared Detection of the Hysteresis in the Thermally Induced Spin-Crossover in Bis(4,4 '-Bis-1,2,4-Triazole)Bis(Thiocyanato-N)Iron(Ii) Monohydrate. *Inorg. Chim. Acta* **2000,** *303*, 287-290.

(31) Zhu, Y.-Y.; Li, H.-Q.; Ding, Z.-Y.; Lü, X.-J.; Meng, Y.-S.; Liu, T.; Gao, S. Spin Transitions in a Series of [Fe(Pybox)2]2+ Complexes Modulated by Ligand Structures, Counter Anions, and Solvents. *Inorg. Chem. Front.* **2016,** *3*, 1624-1636.

(32) Elhaïk, J.; Kilner, C. A.; Halcrow, M. A. Structural Diversity in Iron(Ii) Complexes of 2,6-Di(Pyrazol-1-Yl)Pyridine and 2,6-Di(3-Methylpyrazol-1-Yl)Pyridine. *Dalton. Trans.* **2006**, 823-830.

(33) Cook, L. J. K.; Shepherd, H. J.; Comyn, T. P.; Baldé, C.; Cespedes, O.; Chastanet, G.; Halcrow, M. A. Decoupled Spin Crossover and Structural Phase Transition in a Molecular Iron(Ii) Complex. *Chem. - Eur. J.* **2015,** *21*, 4805-4816.

(34) Shiga, T.; Saiki, R.; Akiyama, L.; Kumai, R.; Natke, D.; Renz, F.; Cameron, J. M.; Newton, G. N.; Oshio, H. A Bronsted-Ligand-Based Iron Complex as a Molecular Switch with Five Accessible States. *Angew Chem Int Edit* **2019,** *58*, 5658-5662.

(35) Sunatsuki, Y.; Ohta, H.; Kojima, M.; Ikuta, Y.; Goto, Y.; Matsumoto, N.; Iijima, S.; Akashi, H.; Kaizaki, S.; Dahan, F.; Tuchagues, J.-P. Supramolecular Spin-Crossover Iron Complexes Based on Imidazole−Imidazolate Hydrogen Bonds. *Inorg. Chem.* **2004,** *43*, 4154-4171.

(36) Matar, S. F.; Guionneau, P.; Chastanet, G. Multiscale Experimental and Theoretical Investigations of Spin Crossover Fe-Ii Complexes: Examples of [Fe(Phen)(2)(Ncs)(2)] and [Fe(Pm-Bia)(2)(Ncs)(2)]. *Int. J. Mol. Sci.* **2015,** *16*, 4007-4027.

(37) Cirera, J.; Via-Nadal, M.; Ruiz, E. Benchmarking Density Functional Methods for Calculation of State Energies of First Row Spin-Crossover Molecules. *Inorg. Chem.* **2018,** *57*, 14097-14105.

(38) Sousa, C.; de Graaf, C.; Rudavskyi, A.; Broer, R. Theoretical Study of the Light-Induced Spin Crossover Mechanism in [Fe(Mtz)(6)](2+) and [Fe(Phen)(3)](2+). *J Phys Chem A* **2017,** *121*, 9720-9727.

(39) Mejia-Rodriguez, D.; Albavera-Mata, A.; Fonseca, E.; Chen, D.-T.; Cheng, H.; Hennig, R. G.; Trickey, S. B. Barriers to Predictive High-Throughput Screening for Spin-Crossover. *Comput. Mater. Sci.* **2022,** *206*, 111161.

(40) Vennelakanti, V.; Taylor, M. G.; Nandy, A.; Duan, C.; Kulik, H. J. Assessing the Performance of Approximate Density Functional Theory on 95 Experimentally Characterized Fe(Ii) Spin Crossover Complexes. *J. Chem. Phys.* **2023,** *159*.

(41) Duan, C.; Chen, S.; Taylor, M. G.; Liu, F.; Kulik, H. J. Machine Learning to Tame Divergent Density Functional Approximations: A New Path to Consensus Materials Design Principles. *Chem. Sci.* **2021,** *12*, 13021-13036.

(42) Taylor, M. G.; Yang, T.; Lin, S.; Nandy, A.; Janet, J. P.; Duan, C.; Kulik, H. J. Seeing Is Believing: Experimental Spin States from Machine Learning Model Structure Predictions. *J. Phys. Chem. A* **2020,** *124*, 3286-3299.

(43) Kohn, W.; Sham, L. J. Self-Consistent Equations Including Exchange and Correlation Effects. *Phys. Rev.* **1965,** *140*, 1133-1138.

(44) Cohen, A. J.; Mori-Sanchez, P.; Yang, W. Challenges for Density Functional Theory. *Chem. Rev.* **2012,** *112*, 289-320.

(45) Geerlings, P.; De Proft, F.; Langenaeker, W. Conceptual Density Functional Theory. *Chem. Rev.* **2003,** *103*, 1793-1873.

(46) Ziegler, T. Approximate Density Functional Theory as a Practical Tool in Molecular Energetics and Dynamics. *Chem. Rev.* **1991,** *91*, 651-667.

(47) Cohen, A. J.; Mori-Sanchez, P.; Yang, W. Fractional Charge Perspective on the Band Gap in Density-Functional Theory. *Physical Review B* **2008,** *77*.

(48) Perdew, J. P.; Parr, R. G.; Levy, M.; Balduz, J. L., Jr. Density-Functional Theory for Fractional Particle Number - Derivative Discontinuities of the Energy. *Phys Rev Lett* **1982,** *49*, 1691-1694.

(49) Yang, W.; Zhang, Y.; Ayers, P. W. Degenerate Ground States and a Fractional Number of Electrons in Density and Reduced Density Matrix Functional Theory. *Phys. Rev. Lett.* **2000,** *84*, 5172-5175.

(50) Cohen, A. J.; Mori-Sanchez, P.; Yang, W. Insights into Current Limitations of Density Functional Theory. *Science* **2008,** *321*, 792-794.

(51) Hollett, J. W.; Gill, P. M. W. The Two Faces of Static Correlation. *J. Chem. Phys.* **2011,** *134*, 114111.

(52) Zhang, D.; Truhlar, D. G. Unmasking Static Correlation Error in Hybrid Kohn-Sham Density Functional Theory. *J. Chem. Theory Comput.* **2020,** *16*, 5432-5440.

(53) Paulsen, H.; Duelund, L.; Winkler, H.; Toftlund, H. a.; Trautwein, A. X. Free Energy of Spin-Crossover Complexes Calculated with Density Functional Methods. *Inorg. Chem.* **2001,** *40*, 2201-2203.

(54) Reiher, M.; Salomon, O.; Hess, B. A. Reparameterization of Hybrid Functionals Based on Energy Differences of States of Different Multiplicity. *Theor. Chem. Acc.* **2001,** *107*, 48-55.

(55) Reiher, M. Theoretical Study of the Fe(Phen)2(Ncs)2 Spin-Crossover Complex with Reparametrized Density Functionals. *Inorg. Chem.* **2002,** *41*, 6928-6935.

(56) Jensen, K. P. Bioinorganic Chemistry Modeled with the Tpssh Density Functional. *Inorg. Chem.* **2008,** *47*, 10357-10365.

(57) Staroverov, V. N.; Scuseria, G. E.; Tao, J.; Perdew, J. P. Comparative Assessment of a New Nonempirical Density Functional: Molecules and Hydrogen-Bonded Complexes. *Journal of Chemical Physics* **2003,** *119*, 12129-12137.

(58) Tao, J.; Perdew, J. P.; Staroverov, V. N.; Scuseria, G. E. Climbing the Density Functional Ladder: Nonempirical Meta–Generalized Gradient Approximation Designed for Molecules and Solids. *Phys. Rev. Lett.* **2003,** *91*, 146401.

(59) Ye, S.; Neese, F. Accurate Modeling of Spin-State Energetics in Spin-Crossover Systems with Modern Density Functional Theory. *Inorg. Chem.* **2010,** *49*, 772-774.

(60) Siig, O. S.; Kepp, K. P. Iron(Ii) and Iron(Iii) Spin Crossover: Toward an Optimal Density Functional. *J Phys Chem A* **2018,** *122*, 4208-4217.

(61) Ruan, S.; Jackson, K. A.; Ruzsinszky, A. Spin-Crossover Complexes: Selfinteraction Correction Vs Density Correction. *The Journal of Chemical Physics* **2023,** *158*, 064303.

(62) Romero, S.; Baruah, T.; Zope, R. R. Spin-State Gaps and Self-Interaction-Corrected Density Functional. *J. Chem. Phys.* **2023,** *158*, 054305.

(63) Zhao, Y.; Truhlar, D. G. A New Local Density Functional for Main-Group Thermochemistry, Transition Metal Bonding, Thermochemical Kinetics, and Noncovalent Interactions. *J. Chem. Phys.* **2006,** *125*, 194101.

(64) Yao, K.; Parkhill, J. Kinetic Energy of Hydrocarbons as a Function of Electron Density and Convolutional Neural Networks. *J. Chem. Theory Comput.* **2016,** *12*, 1139-1147.

(65) Snyder, J. C.; Rupp, M.; Hansen, K.; Blooston, L.; Müller, K.-R.; Burke, K. Orbital-Free Bond Breaking Via Machine Learning. *J. Chem. Phys.* **2013,** *139*, 224104.

(66) Häse, F.; Valleau, S.; Pyzer-Knapp, E.; Aspuru-Guzik, A. Machine Learning Exciton Dynamics. *Chem. Sci.* **2016,** *7*, 5139-5147.

(67) Li, Z.; Kermode, J. R.; De Vita, A. Molecular Dynamics with on-the-Fly Machine Learning of Quantum-Mechanical Forces. *Phys. Rev. Lett.* **2015,** *114*, 096405.

(68) Botu, V.; Ramprasad, R. Adaptive Machine Learning Framework to Accelerate Molecular Dynamics. *Int. J. Quantum Chem.* **2015,** *115*, 1074-1083.

(69) Ma, X.; Li, Z.; Achenie, L. E. K.; Xin, H. Machine-Learning-Augmented Chemisorption Model for Co2 Electroreduction Catalyst Screening. *J. Phys. Chem. Lett.* **2016,** *6*, 3528-3533.

(70) Li, Z.; Ma, X.; Xin, H. Feature Engineering of Machine-Learning Chemisorption Models for Catalyst Design. *Catal. Today* **2017,** *280*, 232-238.

(71) Goldsmith, B. R.; Esterhuizen, J.; Liu, J.-X.; Bartel, C. J.; Sutton, C. Machine Learning for Heterogeneous Catalyst Design and Discovery. *AIChE J.* **2018,** *64*, 2311-2323.

(72) Lamoureux, P. S.; Winther, K. T.; Torres, J. A. G.; Streibel, V.; Zhao, M.; Bajdich, M.; Abild-Pedersen, F.; Bligaard, T. Machine Learning for Computational Heterogeneous Catalysis. *ChemCatChem* **2019,** *11*, 3579-3599.

(73) Kitchin, J. R. Machine Learning in Catalysis. *Nat. Catal.* **2018,** *1*, 230-232.

(74)   Meredig, B.; Agrawal, A.; Kirklin, S.; Saal, J. E.; Doak, J. W.; Thompson, A.; Zhang, K.; Choudhary, A.; Wolverton, C. Combinatorial Screening for New Materials in Unconstrained Composition Space with Machine Learning. *Phys. Rev. B* **2014,** *89*, 094104.

(75)   Mannodi-Kanakkithodi, A.; Pilania, G.; Huan, T. D.; Lookman, T.; Ramprasad, R. Machine Learning Strategy for Accelerated Design of Polymer Dielectrics. *Sci. Rep.* **2016,** *6*, 20952.

(76)   Huan, T. D.; Mannodi-Kanakkithodi, A.; Ramprasad, R. Accelerated Materials Property Predictions and Design Using Motif-Based Fingerprints. *Phys. Rev. B* **2015,** *92*, 014106.

(77)   Pyzer-Knapp, E. O.; Li, K.; Aspuru-Guzik, A. Learning from the Harvard Clean Energy Project: The Use of Neural Networks to Accelerate Materials Discovery. *Adv. Funct. Mater.* **2015,** *25*, 6495-6502.

(78)   Lunghi, A.; Sanvito, S. A Unified Picture of the Covalent Bond within Quantum-Accurate Force Fields: From Organic Molecules to Metallic Complexes' Reactivity. *Sci. Adv.* **2019,** *5*, eaaw2210.

(79)   Lunghi, A.; Sanvito, S. Computational Design of Magnetic Molecules and Their Environment Using Quantum Chemistry, Machine Learning and Multiscale Simulations. *Nat. Rev. Chem.* **2022,** *6*, 761-781.

(80)   Smith, J. S.; Isayev, O.; Roitberg, A. E. Ani-1: An Extensible Neural Network Potential with Dft Accuracy at Force Field Computational Cost. *Chem. Sci.* **2017,** *8*, 3192-3203.

(81)   Behler, J. Representing Potential Energy Surfaces by High-Dimensional Neural Network Potentials. *J. Phys.: Condens.Matter* **2014,** *26*, 183001.

(82)   Lorenz, S.; Gross, A.; Scheffler, M. Representing High-Dimensional Potential-Energy Surfaces for Reactions at Surfaces by Neural Networks. *Chem. Phys. Lett.* **2004,** *395*, 210-215.

(83)   Artrith, N.; Morawietz, T.; Behler, J. High-Dimensional Neural-Network Potentials for Multicomponent Systems: Applications to Zinc Oxide. *Phys. Rev. B* **2011,** *83*, 153101.

(84)   Behler, J.; Parrinello, M. Generalized Neural-Network Representation of High-Dimensional Potential-Energy Surfaces. *Phys. Rev. Lett.* **2007,** *98*, 146401.

(85)   Prudente, F. V.; Neto, J. J. S. The Fitting of Potential Energy Surfaces Using Neural Networks. Application to the Study of the Photodissociation Processes. *Chem. Phys. Lett.* **1998,** *287*, 585-589.

(86)   Yao, K.; Herr, J. E.; Parkhill, J. The Many-Body Expansion Combined with Neural Networks. *J. Chem. Phys.* **2017,** *146*, 014106.

(87)   Nguyen, T. T.; Székely, E.; Imbalzano, G.; Behler, J.; Csányi, G.; Ceriotti, M.; Götz, A. W.; Paesani, F. Comparison of Permutationally Invariant Polynomials, Neural Networks, and Gaussian Approximation Potentials in Representing Water Interactions through Many-Body Expansions. *J Chem Phys* **2018,** *148*, 241725.

(88)   Pilania, G.; Gubernatis, J. E.; Lookman, T. Multi-Fidelity Machine Learning Models for Accurate Bandgap Predictions of Solids. *Comput. Mater. Sci.* **2017,** *129*, 156-163.

(89)   Pilania, G.; Mannodi-Kanakkithodi, A.; Uberuaga, B. P.; Ramprasad, R.; Gubernatis, J. E.; Lookman, T. Machine Learning Bandgaps of Double Perovskites. *Sci Rep-Uk* **2016,** *6*.

(90)   Zhuo, Y.; Tehrani, A. M.; Brgoch, J. Predicting the Band Gaps of Inorganic Solids by Machine Learning. *J. Phys. Chem. Lett.* **2018,** *9*, 1668-1673.

(91)   Sifain, A. E.; Lystrom, L.; Messerly, R. A.; Smith, J. S.; Nebgen, B.; Barros, K.; Tretiak, S.; Lubbers, N.; Gifford, B. J. Predicting Phosphorescence Energies and Inferring Wavefunction Localization with Machine Learning. *Chem. Sci.* **2021,** *12*, 10207-10217.

(92) Gómez-Bombarelli, R.; Aguilera-Iparraguirre, J.; Hirzel, T. D.; Duvenaud, D.; Maclaurin, D.; Blood-Forsythe, M. A.; Chae, H. S.; Einzinger, M.; Ha, D.-G.; Wu, T.; Markopoulos, G.; Jeon, S.; Kang, H.; Miyazaki, H.; Numata, M.; Kim, S.; Huang, W.; Hong, S. I.; Baldo, M.; Adams, R. P.; Aspuru-Guzik, A. Design of Efficient Molecular Organic Light-Emitting Diodes by a High-Throughput Virtual Screening and Experimental Approach. *Nat. Mater.* **2016,** *15*, 1120-1127.

(93) Behler, J. Perspective: Machine Learning Potentials for Atomistic Simulations. *J. Chem. Phys.* **2016,** *145*, 170901.

(94) Janet, J. P.; Kulik, H. J. Resolving Transition Metal Chemical Space: Feature Selection for Machine Learning and Structure-Property Relationships. *J. Phys. Chem. A* **2017,** *121*, 8939-8954.

(95) Janet, J. P.; Gani, T. Z. H.; Steeves, A. H.; Ioannidis, E. I.; Kulik, H. J. Leveraging Cheminformatics Strategies for Inorganic Discovery: Application to Redox Potential Design. *Ind. Eng. Chem. Res.* **2017,** *56*, 4898-4910.

(96) Schütt, K. T.; Glawe, H.; Brockherde, F.; Sanna, A.; Müller, K. R.; Gross, E. K. U. How to Represent Crystal Structures for Machine Learning: Towards Fast Prediction of Electronic Properties. *Phys. Rev. B* **2014,** *89*, 205118.

(97) Grisafi, A.; Fabrizio, A.; Meyer, B.; Wilkins, D. M.; Corminboeuf, C.; Ceriotti, M. Transferable Machine-Learning Model of the Electron Density. *ACS Central Science* **2019,** *5*, 57-64.

(98) Fedik, N.; Zubatyuk, R.; Kulichenko, M.; Lubbers, N.; Smith, J. S.; Nebgen, B.; Messerly, R.; Li, Y. W.; Boldyrev, A. I.; Barros, K.; Isayev, O.; Tretiak, S. Extending Machine Learning Beyond Interatomic Potentials for Predicting Molecular Properties. *Nat. Rev. Chem.* **2022,** *6*, 653-672.

(99) Zubatyuk, R.; Smith, J. S.; Nebgen, B. T.; Tretiak, S.; Isayev, O. Teaching a Neural Network to Attach and Detach Electrons from Molecules. *Nat. Commun.* **2021,** *12*, 4870.

(100) Dral, P. O.; Barbatti, M. Molecular Excited States through a Machine Learning Lens. *Nat. Rev. Chem.* **2021,** *5*, 388-405.

(101) Vela, S.; Fumanal, M.; Sousa, C. Understanding Kinetically Controlled Spin Transitions in Bistable Spin Crossover Materials. *J. Mater. Chem. C* **2022,** *11*, 235-243.

(102) Janet, J. P.; Kulik, H. J. Predicting Electronic Structure Properties of Transition Metal Complexes with Neural Networks. *Chem. Sci.* **2017,** *8*, 5137-5152.

(103) Eckhoff, M.; Behler, J. High-Dimensional Neural Network Potentials for Magnetic Systems Using Spin-Dependent Atom-Centered Symmetry Functions. *npj Comput. Mater.* **2021,** *7*, 170.

(104) Merker, H. A.; Heiberger, H.; Nguyen, L.; Liu, T.; Chen, Z.; Andrejevic, N.; Drucker, N. C.; Okabe, R.; Kim, S. E.; Wang, Y.; Smidt, T.; Li, M. Machine Learning Magnetism Classifiers from Atomic Coordinates. *Iscience* **2022,** *25*.

(105) Janet, J. P.; Chan, L.; Kulik, H. J. Accelerating Chemical Discovery with Machine Learning: Simulated Evolution of Spin Crossover Complexes with an Artificial Neural Network. *J. Phys. Chem. Lett.* **2018,** *9*, 1064-1071.

(106) Allen, A. E. A.; Tkatchenko, A. Machine Learning of Material Properties: Predictive and Interpretable Multilinear Models. *Sci. Adv.* **2022,** *8*, eabm7185.

(107) Zhang, W.; Berthebaud, D.; Halet, J.-F.; Mori, T. Electronic Configurations of 3d Transition-Metal Compounds Using Local Structure and Neural Networks. *J Phys Chem A* **2022,** *126*, 7373–7381.

(108) Nandy, A.; Duan, C.; Janet, J. P.; Gugler, S.; Kulik, H. J. Strategies and Software for Machine Learning Accelerated Discovery in Transition Metal Chemistry. *Ind. Eng. Chem. Res.* **2018,** *57*, 13973-13986.

(109) Janet, J. P.; Liu, F.; Nandy, A.; Duan, C.; Yang, T.; Lin, S.; Kulik, H. J. Designing in the Face of Uncertainty: Exploiting Electronic Structure and Machine Learning Models for Discovery in Inorganic Chemistry. *Inorg. Chem.* **2019,** *58*, 10592-10606.

(110) Janet, J. P.; Ramesh, S.; Duan, C.; Kulik, H. J. Accurate Multiobjective Design in a Space of Millions of Transition Metal Complexes with Neural-Network-Driven Efficient Global Optimization. *ACS Central Science* **2020,** *6*, 513-524.

(111) Virshup, A. M.; Contreras-Garcia, J.; Wipf, P.; Yang, W.; Beratan, D. N. Stochastic Voyages into Uncharted Chemical Space Produce a Representative Library of All Possible Drug-Like Compounds. *J. Am. Chem. Soc.* **2013,** *135*, 7296-7303.

(112) Broto, P.; Moreau, G.; Vandycke, C. Molecular Structures: Perception, Autocorrelation Descriptor and Sar Studies. System of Atomic Contributions for the Calculation of the N-Octanol/Water Partition-Coefficients. *Eur. J. Med. Chem.* **1984,** *19*, 71-78.

(113) Broto, P.; Devillers, J. *Autocorrelation of Properties Distributed on Molecular Graphs*, 1990.

(114) Devillers, J.; Domine, D.; Guillon, C.; Bintein, S.; Karcher, W. Prediction of Partition Coefficients (Log P Oct) Using Autocorrelation Descriptors. *SAR QSAR Environ. Res.* **1997,** *7*, 151-172.

(115) Breiman, L. Random Forests. *Mach. Learn.* **2001,** *45*, 5-32.

(116) Liu, F.; Duan, C.; Kulik, H. J. Rapid Detection of Strong Correlation with Machine Learning for Transition-Metal Complex High-Throughput Screening. *J. Phys. Chem. Lett.* **2020,** *11*, 8067-8076.

(117) Pedregosa, F.; Varoquaux, G.; Gramfort, A.; Michel, V.; Thirion, B.; Grisel, O.; Blondel, M.; Prettenhofer, P.; Weiss, R.; Dubourg, V.; Vanderplas, J.; Passos, A.; Cournapeau, D.; Brucher, M.; Perrot, M.; Duchesnay, E. Scikit-Learn: Machine Learning in Python. *J Mach Learn Res* **2011,** *12*, 2825-2830.

(118) Guyon, I. An Introduction to Variable and Feature Selection. *J. Mach. Learn. Res.* **2003,** *3*, 1157– 1182.

(119) Genuer, R.; Poggi, J.-M.; Tuleau-Malot, C. Variable Selection Using Random Forests. *Pattern Recogn. Lett.* **2010,** *31*, 2225-2236.

(120) Bergstra, J.; Yamins, D.; Cox, D. D. Hyperopt: A Python Library for Optimizing the Hyperparameters of Machine Learning Algorithms. *Proceedings of the 12th Python in Science Conference* **2013**, 13.

(121) Groom, C. R.; Bruno, I. J.; Lightfoot, M. P.; Ward, S. C. The Cambridge Structural Database. *Acta Crystallographica Section B-Structural Science Crystal Engineering and Materials* **2016,** *72*, 171-179.

(122) Perdew, J. P.; Schmidt, K. Jacob's Ladder of Density Functional Approximations for the Exchange-Correlation Energy. *AIP Conference Proceedings* **2001,** *577*, 1.

(123) Shvachko, Y. N.; Starichenko, D. V.; Korolyov, A. V.; Yagubskii, E. B.; Kotov, A. I.; Buravov, L. I.; Lyssenko, K. A.; Zverev, V. N.; Simonov, S. V.; Zorina, L. V.; Shakirova, O. G.; Lavrenovag, L. G. The Conducting Spin-Crossover Compound Combining Fe(Ii) Cation Complex with Tcnq in a Fractional Reduction State. *Inorg. Chem.* **2016,** *55*, 9121-9130.

(124) Hagiwara, H.; Tanakaa, T.; Hora, S. Synthesis, Structure, and Spin Crossover above Room Temperature of a Mononuclear and Related Dinuclear Double Helicate Iron(Ii) Complexes. *Dalton. Trans.* **2016,** *45*, 17132-17140.

(125) Benaicha, B.; Do, K. V.; Yangul, A.; Pittala, N.; Lusson, A.; Sy, M.; Bouchez, G.; Fourati, H.; Gómez-García, C. J.; Triki, S.; Boukheddaden, K. Interplay between Spin-Crossover and Luminescence in a Multifunctional Single Crystal Iron(Ii) Complex: Towards a New Generation of Molecular Sensors. *Chem. Sci.* **2019,** *10*, 6791-6798.

(126) Li, L.; Neville, S. M.; Craze, A. R.; Clegg, J. K.; Sciortino, N. F.; Arachchige, K. S. A.; Mustonen, O.; Marjo, C. E.; Mcrae, C. R.; Kepert, C. J.; Lindoy, L. F.; Aldrich-Wright, J. R.; Li, F. Spin-State Patterning in an Iron(Ii) Tripodal Spin-Crossover Complex. *ACS Omega* **2017,** *2*, 3349-3353.

(127) Ishida, T.; Kanetomo, T.; Yamasaki, M. An Iron(Ii) Complex Tripodally Chelated with 1,1,1-Tris(Pyridin-2-Yl)Ethane Showing Room-Temperature Spin-Crossover Behaviour. *Acta Crystallogr., Sect. C: Struct. Chem.* **2016,** *72*, 797-801.

(128) Sugaya, T.; Fujihara, T.; Naka, T.; Furubayashi, T.; Matsushita, A.; Isago, H.; Nagasawa, A. Observation of the First Spin Crossover in an Iron(Ii) Complex with an S6 Coordination Environment: Tris[Bis(N,N-Diethylamino)Carbeniumdithiocarboxylato]Iron(Ii) Hexafluorophosphate. *Chem. - Eur. J.* **2018,** *24*, 17955-17963.

(129) Han, W.-K.; Qin, L.-F.; Pang, C.-Y.; Cheng, C.-K.; Zhu, W.; Li, Z.-H.; Li, Z.; Ren, X.; Gu, Z.-G. Polymorphism of a Chiral Iron(Ii) Complex: Spin-Crossover and Ferroelectric Properties. *Dalton. Trans.* **2017,** *46*, 8004-8008.

(130) Dova, E.; Peschar, R.; Sakata, M.; Kato, K.; Schenk, H. High-Spin- and Low-Spin-State Structures of [Fe(Chloroethyltetrazole)6](Clo4)2 from Synchrotron Powder Diffraction Data. *Chem. - Eur. J.* **2006,** *12*, 5043-5052.

(131) Struch, N.; Wagner, N.; Schnakenburg, G.; Weisbarth, R.; Klos, S.; Beck, J.; Lützen, A. Thiazolylimines as Novel Ligand-Systems for Spin-Crossover Centred near Room Temperature. *Dalton. Trans.* **2016,** *45*, 14023-14029.

(132) García-López, V.; Palacios-Corella, M.; Gironés-Pérez, V.; Bartual-Murgui, C.; Real, J. A.; Pellegrin, E.; Herrero-Martín, J.; Aromí, G.; Clemente-León, M.; Coronado, E. Heteroleptic Iron(Ii) Spin-Crossover Complexes Based on a 2,6-Bis(Pyrazol-1-Yl)Pyridine-Type Ligand Functionalized with a Carboxylic Acid. *Inorg. Chem.* **2019,** *58*, 12199-12208.

(133) Ye, Y. S.; Chen, X. Q.; Cai, Y. D.; Fei, B.; Dechambenoit, P.; Rouzieres, M.; Mathoniere, C.; Clerac, R.; Bao, X. Slow Dynamics of the Spin-Crossover Process in an Apparent High-Spin Mononuclear Fe-Ii Complex. *Angew. Chem., Int. Ed.* **2019,** *58*, 18888-18891.

(134) Jornet-Molla, V.; Duan, Y.; Gimenez-Saiz, C.; Tang, Y.-Y.; Li, P.-F.; Romero, F. M.; Xiong, R.-G. A Ferroelectric Iron(Ii) Spin Crossover Material. *Angew. Chem., Int. Ed.* **2017,** *56*, 14052-14056.

(135) Mörtel, M.; Witt, A.; Heinemann, F. W.; Bochmann, S.; Bachmann, J.; Khusniyarov, M. M. Synthesis, Characterization, and Properties of Iron(Ii) Spin-Crossover Molecular Photoswitches Functioning at Room Temperature. *Inorg. Chem.* **2017,** *56*, 13174-13186.

(136) Hrudka, J. J.; Phan, H.; Lengyel, J.; Rogachev, A. Y.; Shatruk, M. Power of Three: Incremental Increase in the Ligand Field Strength of N-Alkylated 2,2′-Biimidazoles Leads to Spin Crossover in Homoleptic Tris-Chelated Fe(Ii) Complexes. *Inorg. Chem.* **2018,** *57*, 5183-5193.

(137) Hasegawa, Y.; Sakamoto, R.; Takahashi, K.; Nishihara, H. Bis[(E)-2,6-Bis(1h-Pyrazol-1-Yl)-4-Styrylpyridine]Iron(Ii) Complex: Relationship between Thermal Spin Crossover and Crystal Solvent. *Inorg. Chem.* **2013,** *52*, 1658-1665.

TOC Graphic